The 5.8 μm absorption bands for nitric acid (H 14 N 16 O 3): line positions and intensities for the ν 2 band at 1709.567 cm –1 and for its first associated hot bands (ν 2 +ν 9 –ν 9 , ν 2 +ν 7 –ν 7 , ν 2 +ν 6 –ν 6)

A. Perrin, L. Manceron, R. Armante, F. Kwabia-Tchana, P. Roy, D. Doizi, G. C. Toon

The 5.8 µm absorption bands for nitric acid ($H^{14}N^{16}O_3$): line positions and intensities for the ν_2 band at 1709.567 cm^{-1} and for its first associated hot bands ($\nu_2+\nu_9-\nu_9$, $\nu_2+\nu_7-\nu_7$, $\nu_2+\nu_6-\nu_6$).

A. Perrin[a,*]

L. Manceron [b,c],

R.Armante [a,]

F. Kwabia-Tchana [d],

P.Roy[b]

D. Doizi [e]

G.C. Toon[f]

This work is dedicated to Dr. Jean-Marie Flaud on the occasion of his 75th birthday

[a]Laboratoire de Météorologie Dynamique/IPSL, UMR CNRS 8539, Ecole Polytechnique, Université Paris-Saclay, RD36, 91128 Palaiseau Cedex, France

.[b] Ligne AILES, Synchrotron SOLEIL, L'Orme des Merisiers, St-Aubin BP48, 91192 Gif-sur-Yvette Cedex, France.

[c] Sorbonne Université, CNRS, MONARIS, UMR 8233, 4 place Jussieu, Paris, F-75005 France

[d] Université de Paris and Univ Paris Est Creteil, CNRS, LISA, F-75013 Paris, France

[e] DEN-Service d'Etude du Comportement des Radionucléides (SECR), CEA, Université Paris-Saclay, F-91191, Gif-sur-Yvette, France

[f] Jet Propulsion Laboratory, California Institute of Technology, Pasadena California, USA

Number of tables: 5

Number of figures: 8

* Corresponding author: agnes.perrin@lmd.ipsl.fr,

Abstract:

This paper is the second of two back-to-back works, whose goal was to generate a more accurate linelist for the 5.8 μm absorption band of HNO_3. Here we report improved line positions and intensities in the ν_2 cold band which is the main band in this region. For this, we recorded four high resolution Fourier transform spectra for the ν_2 band, centered at 1709.567 cm^{-1}, under different experimental conditions. Using these spectra, a new extended line position analysis was performed for the ν_2 band, leading to more accurate line positions. In parallel, individual line intensities were measured. It appears that, although the ν_2 band is mainly of B-type, it also possesses a (very) weak A-type component that cannot be ignored. Overall, the line intensities in this new database are about 8% weaker than those quoted presently in the HITRAN (https://hitran.org/) or GEISA (https://geisa.aeris-data.fr/) databases. Our final linelist for HNO_3 at 5.8 μm is provided as a supplement to this paper. It includes lines from the ν_2 band together with those of the $\nu_2+\nu_9-\nu_9$, $\nu_2+\nu_6-\nu_6$, and $\nu_2+\nu_7-\nu_7$ associated hot bands that were generated during the first part of this study, described in the companion paper.

I Introduction

This paper is the second of two back-to-back works, whose goal is to update the existing line positions and intensities spectroscopic parameters for the 5.8 μm band of nitric acid in the HITRAN [1] or GEISA [2] spectroscopic databases. This study is devoted to the positions and intensities for the ν_2 band centered at 1709.567 cm^{-1}, while the first one [3] dealt with the first generation of linelists for the $\nu_2+\nu_9-\nu_9$, $\nu_2+\nu_7-\nu_7$, and $\nu_2+\nu_6-\nu_6$ hot bands at 5.8 μm.

Nitric acid has its strongest infrared signature in the 11 μm, 7.6 μm and 5.8 μm regions corresponding mainly to the $\{\nu_5,2\nu_9\}$, $\{\nu_3,\nu_4\}$ and ν_2 bands, respectively. As far as satellite instruments are concerned, these three spectral ranges of absorption are covered by the late Michelson Interferometer for Passive Atmospheric Sounding (MIPAS) limb emission radiances MIPAS instrument [4], by the ACE-FTS [5] and by the IASI instruments [6]. This will continue to be the case for the future IASI-NG (Infrared Atmospheric Sounder Interferometer - New Generation) instrument that will be launched soon on the new generation of the METOP satellite [7].

The relative band intensities of these three absorption bands are known thanks to the integrated absorption cross-sections measured by Chackerian et al. [8] :

$$I(11\ \mu m) : I(7.6\ \mu m) : I(5.8\ \mu m) = 1.00 : 2.1 : 2.4 \qquad \text{Eq.(1)}$$

In fact, □2 is, by far, the strongest vibrational band of HNO_3 because, in the 7.6 µm region, the line intensities are shared by the strong ν_3 and ν_4 bands and by several dark bands. There exist lists of line-by-line parameters for nitric acid in the publically-accessible HITRAN (https://hitran.org/) [1] or GEISA databases (https://geisa.aeris-data.fr/) [2] for these three spectral regions. Among these, the 11 µm band, falling in a rather clear atmospheric window but about half the strength of the others, was the subject of the first updates and validations [9, 10, 11] because of its practical interest. More recently, the 7.6 µm bands were also the subject of several studies [12, 13]. At 11 µm and 7.6 µm, the linelists, which are now included in the present versions of the HITRAN [1] and GEISA [2] databases, concern the main cold bands, together with, when possible, some of their first associated hot bands.

The present work focusses on the 5.8 µm absorption band of HNO_3. In tropospheric spectra, this HNO_3 signature, which is almost completely masked by interfering absorption of water vapor, cannot be used for HNO_3 retrievals in the troposphere. However, in the stratosphere, this HNO_3 signature is quite observable, for instance it stands out in the very high resolution (0.002-cm^{-1} full width at half maximum (FWHM)) solar occultation spectra recorded at 32°N latitude at 37 km altitude with a balloon-borne interferometer of the University of Denver [15]. Also, this spectral range is of potential use for the ACE-FTS instrument [5] and for the MkIV balloon-borne instrument of the JPL laboratory [14]. In addition, in atmospheric spectra, the 5.8 µm band of HNO_3 is partially overlapping the H_2CO signature in the ν_2 band region (1746 cm^{-1}). The strongest IR bands of Peroxy Acetyl Nitrate (PAN) and of acetone are located at 1740 cm^{-1}, strongly overlapping the ν_2 HNO_3 band. Therefore, availability of good line parameters for HNO_3 in this spectral region is important for atmospheric retrieval of these other gases. Let us mention that, contrary to what exists for the 11 µm and 7.6 µm regions, the HNO_3 linelist in HITRAN and GEISA at 5.8 µm, hereafter labelled as “HITRAN-GEISA”, currently includes only parameters of the ν_2 (cold) band of HNO_3.

Recently, G. Toon [16] pointed out that the “HITRAN-GEISA” linelist at 5.8 µm cannot reproduce correctly the HNO_3 infrared signature in stratospheric spectra. This observation was performed using balloon-borne solar spectra recorded by the MkIV instrument [14] in the lower

stratosphere, therefore for a low temperature (about 200K). This anomalous behavior cannot be due to the contribution of hot bands, which up to now are still missing in the HITRAN and GEISA databases, since the same mismatch is observed when trying to reproduce the Pacific Northwest National Laboratory (PNNL) cross sections recorded at 296K [8, 17].

Before going to the description of the present work it is necessary to describe the origin of the existing line parameters in the public databases.

Literature data in line positions and intensities:

According to symmetry considerations for a planar C_s- type molecule, the ν_2 band is a hybrid band, with both B- and A-type transitions, with (ΔK_a= odd, ΔK_c=odd) and (ΔK_a= even, ΔK_c= odd) selection rules on the K_a and K_c rotational quantum numbers, respectively. However, up to now, only B- type transitions were observed for the ν_2 band.

The first laboratory measurement of this band was performed by A. Maki [18] using diode laser spectroscopy in the 1688 to 1737 cm^{-1} spectral region. Later, a more complete investigation of the ν_2 band was performed by Tan et al. [19] using high resolution Fourier transform spectra. In this way 4459 B-type transitions were identified, involving rotational quantum numbers up to $J \leq 72$ and $K_a \leq 45$. Most of the ν_2 transitions appear unperturbed and could be reproduced satisfactorily using an A-type Watson-type Hamiltonian written in Ir reduction [20]. However, both Maki [18] and Tan et al. [19] noticed that several local resonances affect transitions in the 1675, 1684, 1730 and 1737 cm^{-1} spectral regions. Therefore, in these two studies, the band center and the set of rotational constants for the 2^1 vibrational state were obtained during a least squares fit calculation performed on the observed transitions, after removing the perturbed lines from that list. Also, the ground state set parameters were maintained fixed at their values obtained in Ref. [21].

As far as the intensities are concerned, there exist several integrated band intensities measurements (IBI) for the 5.8 μm absorption band of nitric acid. [22, 23, 8]. The IBI value provided by Chackerian et al. [8] in the 5.8 μm absorption band does not differ significantly from the value provided by Giver et al. [23]. On the other hand, Goldman's values [22], measured at a lower resolution and for a rather shorter absorption cell than these latest ones, are about 8% to 10% weaker. Hereafter, we will refer to the value provided by Chackerian et al. [8], which is:

$^{Low}S_{Tot}^{5.8\mu m}$ (296K) = 5.71(19)×10^{-17} cm^{-1}/(molecule.cm^{-2}) at 296 K, [8] Eq.(2)

To our knowledge, the only existing line by line measurements, of several small portions of the ν_2 R branch, were performed by Bair et al. [24] and May et al. [25] using diode laser techniques.

One of the main problems to solve was to describe more precisely the line intensity pattern of the ν_2 band. Obviously, this band differs from the much-too-simple description adopted during the previous studies, i.e. a pure B- type band, with no centrifugal distortion effects in the description of the ν_2 transition moment operator. To improve this situation we needed, as input data for our calculations, a large set of individual line intensities measurements in the P, Q and R branches of the ν_2 band.

Status of the HNO_3 linelist at 5.8 µm in HITRAN and GEISA

At 5.8 µm, the HITRAN and GEISA linelists include only parameters for the ν_2 cold band of $H^{14}N^{16}O_3$. In these databases, the ν_2 line positions were generated in Ref. [15] using an A-type Watson I^r reduced rotational Hamiltonian, and the (0) lower and (2^1) upper state energy levels were computed using the ground and upper state parameters collected in Refs. [21] and [19], respectively. Most of the lines are not affected by vibration rotation resonances. However, for the ν_2 perturbed lines the computed line positions in the HITRAN-GEISA database [1, 2] can differ from those observed, because no specific treatment was adopted during the line positions computation.

The line intensities (in cm^{-1}/(molecule.cm^{-2}) at 296K for the $H^{14}N^{16}O_3$ (main) isotopic species in a natural sample of nitric acid, were computed using the usual expression:

$$k_{\tilde{\nu}}^{N}(T) = a_{iso}\frac{8\pi^3\tilde{\nu}}{4\pi\epsilon_0 3hc}exp\left(-\frac{E_L}{kT}\right)\left(1-exp\left(\frac{hc\tilde{\nu}}{kt}\right)\right)\frac{1}{Z(T)}R_L^U \qquad \text{Eq.(3)}$$

In this expression L and U are respectively the lower and upper levels of the transition, $\tilde{\nu} = (E_U - E_L)/hc$ is the wavenumber of the transition in cm^{-1}. Also, $a_{Iso} = 0.989110$ is the isotopic fraction of the considered $H^{14}N^{16}O_3$ species assumed in our computation, as usual in HITRAN and GEISA, for a natural sample of nitric acid. In addition, $Z_{tot}(T)$ is the total partition function:

$$Z_{tot}(T)=Z_{vib}(T)\times Z_{rot}(T), \qquad \text{Eq.(4)}$$

which includes a vibrational $Z_{vib}(T)$ and rotational part $Z_{rot}(T)$.

During this work, we used the values:

$Z_{vib}(223K)=1.10965$, $Z_{rot}(223K)=17909.61$ and then $Z_{tot}(223K)= 19874.19$,

$Z_{vib}(250K)=1.11673$, $Z_{rot}(250K)= 21258.47$ and then $Z_{tot}(250K)= 24815.80$,

$Z_{vib}(296K)= 1.29952$, $Z_{rot}(296K)= 27390.91$, and then $Z_{tot}(296K)= 35595.09$. Eq.(5)

at 223K, 250K and 296K, respectively.

Finally, R_L^U is the square of the matrix element of the transformed dipole moment operator, which, for the ν_2 isolated band, takes the following form:

$$R_L^U = \left|\left\langle v'=2, J'K_a'K_c' \left| {}^{2,0}\mu_Z' \right| 0, J''K_a''K_c'' \right\rangle\right|^2, \qquad \text{Eq. (6)}$$

In the HITRAN or GEISA linelist, this line intensity computation was performed considering that band as a pure B-type band. As no distortion effect was considered in the description of the ν_2 band transition moment operator, ${}^2\mu_Z'$ was restricted to its first order term for a pure B-type band:

$${}^{2,0}\mu_Z' = {}^{2,0}\mu_1^B \times \phi_{x=B}, \qquad \text{Eq. (7)}$$

In this expression, $\varphi_{x=B}$ is the direction cosine between the Z- laboratory fixed and the x=B molecular fixed axes, and μ_1^B is the zero-order intensity parameter.

For the ν_2 line list currently in HITRAN and GEISA, the ν_2 line intensities were generated using a μ_1^B value that was adjusted to bring the integrated band intensity at 5.8 μm to the value provided by Chackerian et al. [8]. According to our computations and to the value of the total partition that we used (see Eq. 5) this leads to the following value for ${}^{2,0}\mu_1^B$:

$$^{2,0}\mu_1^B \approx 0.283 \text{ Debye.}^{1} \qquad \text{Eq. (8)}$$

Indeed, by summing the individual ν_2 line intensities in the HITRAN-GEISA linelist it is possible to compute $^{HIT-GEIS}S_{\nu 2}(296K)$, which is the ν_2 band intensity.

$$^{HIT-GEIS}S_{\nu 2}(296K) = 4.38\times10^{-17} \text{ cm}^{-1}/(\text{molecule.cm}^{-2}) \text{ at 296 K,} \qquad \text{Eq.(9)}$$

This ν_2 band intensity is linked to the (IBI) $^{Low}S_{Tot}^{5.8\mu m}(296K)$ integrated band intensity at 5.8 µm (see Eq. 2) by the following expression [10]:

$$S_{Tot}^{5.8\mu m}(296K) \approx {}^{HIT-GEIS}S_{\nu 2}(296K) \times Z_{vib}(296K)/a_{Iso} \qquad \text{Eq.(10)}$$

In Eq.(10), the $Z_{vib}(296)$ is the vibrational partition function ($Z_{vib}(296)$=1.29952 at 296K). This is because the (IBI) $^{Low}S_{Tot}^{5.8\mu m}(296K)$ integrated band intensity at 5.8 µm includes contributions from the hot bands associated to the ν_2 band, and from those of other minor isotopic species.

Overview:

The purpose of the present study was to generate a list of better quality for the 5.8 µm absorption band. This new list, hereafter labelled as "GEISA-21", which will be included in the 2021 release of the GEISA database, corresponds to an improved version of the ν_2 band of HNO_3 which, we hope, will solve the observed problem in stratospheric spectra. First, we improved line positions and intensities in the ν_2 cold band which is the main cold band in this region. For this, we recorded four high resolution Fourier transform spectra for the ν_2 band at 1709.567 cm^{-1} (5.8 µm region) in different experimental conditions. Using these spectra, a new extended line position analysis was performed for the ν_2 band, leading to accurate line position parameters. In parallel, individual line intensities were measured for the ν_2 band. It appeared that for the mainly B-type ν_2 band, the existence of a (very) small A-type component

[1] 1 Debye =3.33564 x10^{-30} C.m. In their papers Maki [18] and Tan et al. [19] use the values $^{2,0}\mu_1^B$= 0.2845 and 0.249 Debye, respectively. We presume that they use a different value of the partition function.

cannot be ignored. The final linelist at 5.8 µm includes lines from the ν_2 band together with those of its first three associated hot bands ($\nu_2+\nu_9-\nu_9$, $\nu_2+\nu_7-\nu_7$, $\nu_2+\nu_6-\nu_6$) which were generated during the first part of this study in the companion paper [3] .

II Experimental details.

The same experimental setup and samples were used here as in the companion paper [3], but, in addition to the two spectra described in that paper, three supplementary high-resolution spectra were acquired at 223(1)K, to minimize decomposition of HNO_3 during spectral recording, interference with hot bands and, incidentally, residual water lines. The data were recorded with the same spectroscopic methods as FTS2 [3] with a resolution of 0.0017 cm^{-1} corresponding to a full width at half maximum of the apparatus sinc function of about 0.0012 cm^{-1}, thus always narrower than the Doppler width (ca. 0.0023 cm^{-1}). Reducing the temperature increased dramatically the sample stability to the extent that only one or two cell fillings were needed. Nevertheless, the problem of adsorption/desorption on the walls was still a difficulty. The cell was thus slowly filled while recording spectra over several hours, keeping the HNO_3 sample in a low temperature bath near -60°C, to reach a stable pressure reading and overall spectrum stability. Next, the data collection involving typically, 256 interferograms, recorded in 1h blocks of 34, was carried out. Each block was separately inspected and compared, taking a region of the R branch with about one hundred lines to test the HNO_3 stability in the cell. In total, data were collected in blocks of 34 scans (1h) over 8 to 12 h (total duration). In this way, the small HNO_3 pressure decrease could be assessed from the decrease of HNO_3 line depths and an average pressure estimated. The HNO_3 lines showed a 7% decrease over 8h and the NO_2 lines grew in. If a longer measurement time was desired, the cell was evacuated and slowly refilled by keeping the sample in the low temperature bath until the initial pressure was reproduced. Using HITRAN parameters [1] the residual H_2O and NO_2 could be estimated and amounted to 2.10^{-4} hPa and 1 to 2.5 10^{-4} hPa, respectively. The estimated HNO_3 pressures for all spectra were corrected accordingly. The spectrum was calibrated by matching the measured positions of residual H_2O to reference wavenumbers available in HITRAN [1] with a root mean square (RMS) deviation of 1.8×10^{-4} cm^{-1}. Given the precision of the reference lines, it is safe to claim a 3×10^{-4} cm^{-1} frequency accuracy. Table 1 summarizes the experimental data for the spectra used during this work. Also, Fig. 1 presents an overview of the four spectra recorded at 5.8 µm.

III Line positions for the ν_2 band

The updated analysis of the ν_2 band was initiated by using predicted line lists (positions and intensities). For the 2^1 excited vibrational state, we could use the (already) excellent parameters achieved during the previous ν_2 investigation [19], while during all this work, we used the parameters of Ref. [26] to compute the rotational energy levels in the ground state.

The assignment process was very easy. More than 4800 lines of the ν_2 band were identified which involve J and K_a values up to $J \leq 74$ and $K_a \leq 59$. This means that the present analysis is slightly more extended than the one performed by Tan et al. [19] ($J \leq 72$ and $K_a \leq 45$).

The ν_2 band is clearly mostly a B-type band. However, in the band center of the ν_2 band, we could identify also several weak "pure A-type" Q-type transitions ($\Delta K_a=0$, $\Delta K_c=\pm 1$). This will be discussed further in the text.

As was case during the previous investigations of this band [18, 19], we noticed that in several series of transitions, the lines were not at the predicted positions. The first perturbed series concern transitions with $J \geq 36$, for $K_c \approx 28$, or $K_c \approx 11$. As during these previous studies, we failed completely to account explicitly for these resonances. Let us mention that the number of dark vibrational states, which can possibly be responsible for the resonances affecting the 2^1 state, is quite large. For nitric acid, seven of its nine vibrational modes correspond to vibrational energies weaker than ν_2, and the fact that the ν_9 mode at 458.2 cm^{-1} is a large amplitude vibrational mode can increase the complexity of the resonance scheme. Furthermore, during the computation of the energy levels of the 4^1 and 3^1 bright vibrational states at 1303.072 and 1326.186 cm^{-1} [12] it was necessary to account for strong vibration-rotation resonances which couple together these energy levels with those from four dark states: 6^2, 9^3, $5^1 9^1$, and $7^1 8^1$.

Therefore, we used the same theoretical model (A-type Watson's type rotational Hamiltonian, written in I^R representation) as in Refs. [18, 19]. The 2^1 set of vibrational band center and rotational constants were determined during a least squares minimization performed on a large set of experimental 2^1 energy levels. As during previous investigations [18, 19], the perturbed energy levels were not included in the calculation. The final set of rovibrational

constants for the 2^1 state is gathered in Table 2, together with their associated errors. For information, this Table also compares the values of the rotational constants achieved during this work to those obtained by Tan et al. [19]. However, this comparison is not really meaningful. First because we use a different set of rotational constants for the ground vibrational state in this work [26] than during the investigations performed in Refs. [19], and Ref. [18]. The second reason is that these 2^1 parameters depend on the set of the presumed "unperturbed" experimental data (the ν_2 line positions in Tan's work, or the 2^1 energy levels in this work), that were introduced in the least squares fit computation. Indeed, we do not have precise information on the selection of the "unperturbed versus perturbed" ν_2 lines that was performed in Ref. [19].

IV Line intensities for the ν_2 (cold) band:

Introduction:

Before going into details of the line intensity measurements, it is important to describe our strategy. Indeed, we presumed at the early stage of this study that the ν_2 band had a (very small) A-type component in addition to its (main) B-type character. The major difference between A- and B-type bands is in the structure of their Q- branches ($\Delta J=0$) for which the stronger lines involve high K_a values. Indeed, for a B-type band (like ν_2) the Q type structures of transitions, with $\Delta J=0$ and $\Delta K_a=\pm1$ selections rules, are scattered in bundles on either side of the ν_2 band center. In contrast, for an A-type band, the transitions with $\Delta J=0$ and $\Delta K_a=0$ selection rules are grouped together in a rather narrow Q branch. When looking at the overall structure of the ν_2 band, it is clear that the central spectral region is clear of strong transitions. Indeed, in the 1708.9 – 1709.7 cm^{-1} spectral range only very weak lines are observable on the actual spectrum. In previous works [18, 19], the a-type transitions were stated too weak to be observable. During the present work we identified some of these lines as belonging to the (weak) A-type component of the Q branch of the ν_2 band. This is evidenced in Fig. 2 which presents the band center in the 1709.5 cm^{-1} region with a clear identification (purple triangles) of the (A-type) $^{Q}Q(K_a=J)$ branch transitions of the ν_2 band.

Line intensity measurements

The intensities for the ν_2 band have been determined in two ways: total integrated band intensities were measured in three spectra corresponding to different pressures of HNO_3. The average band intensity at 223K is extracted from the slope of the variation of the integrated intensity with pressure, yielding a value of $5.1(3)\times10^{-17}$ of $cm^{-1}/(molecule.cm^{-2})$. The integration was carried out between 1655 and 1756 cm^{-1}, taking the baseline as the straight line interpolated between the noise average on the 1562-1567 and the 1796-1801 cm^{-1} intervals. The uncertainty is estimated from the relative uncertainties of pressure, temperature and path length, supposing also 3% uncertainty on the individual integrated intensities, twice the slight variations obtained in varying the integration limits and methods for interpolating the baseline. This value is to be compared to $5.71(19)\times10^{-17}$ in reference [8], note that the difference between the measurements is slightly larger than the sum of the combined error bars. The second method involves fitting, after a factor-four post zero-filling, selected relatively isolated spectral lines using either the WSpectra [27] or OPUS software, the first taking explicitly into account the interferometer apparatus function in the intensity retrieval. Here, at the pressure used, lines are found to have Gaussian profiles within the measurement noise and the differences found between the fit results obtained with either software were found to be very small (about one percent) compared to the uncertainty due to the other sources of error (precision of the fit itself, measurement noise, pressure and temperature uncertainties). Each line was fitted separately for each of the three pressures and the retrieved line intensities at 223K were averaged. The temperature and pressures are measured with a relative uncertainty of 0.9% and 5.8 to 1.7%, respectively. To this, we added a somewhat arbitrarily determined uncertainty linked to the precision of the fit, varying from 5% for strong lines to 15% for the weakest. Note, however, that these uncertainty values are not completely arbitrary, as they reflect the range of intensities retrieved for the same line at the three different pressures. These uncertainty values presented in the Table 3 below represent the sum of these relative uncertainties. An example of the fit for lines of the three branches is given in Figure 3.

Line intensity calculations

The 158 experimental intensities measured during this work for a “pure” isotopic sample of $H^{14}N^{16}O_3$ were introduced in a least squares fit calculation to get the expansion of the ν_2 transition moment operator. This expansion, which includes both B-type and A-type components, was set up as:

$$^{2,0}\mu'_Z = {}^{2,0}\mu_1^B \times \varphi_x + {}^{2,0}\mu_2^B \times \varphi_x \mathbf{J}^2 + {}^{2,0}\mu_2^A \times \varphi_z + {}^{2,0}\mu_4^A \times 1/2\left(\{\varphi_x, iJ_y\} + \{i\varphi_y, J_x\}\right) \quad \text{Eq.(11)}$$

The resulting $^{2,0}\mu_i^{A\ or\ B}$ (i=1 to 4) values appearing in this expansion of $^{2,0}\mu'_Z$ are given, together with their estimated uncertainties, in Table 4. The list of 158 measured intensities, together with the results of the calculations, is provided in Table 3.

V Computation of synthetic spectra (line position and intensities)

Synthetic spectra in the 5.8 µm spectral region

We next generated the "GEISA-21" list of line positions and intensities for the ν_2 band together those of the $\nu_2+\nu_9-\nu_9$, $\nu_2+\nu_6-\nu_6$, and $\nu_2+\nu_7-\nu_7$ associated hot bands. The ν_2 line positions were computed using the band centers and rotational constants listed in Tables 2 and in Ref. [26] for the upper 2^1 and the ground states, respectively. As far as the line positions are concerned, the computation of the $\nu_2+\nu_9-\nu_9$, $\nu_2+\nu_6-\nu_6$, and $\nu_2+\nu_7-\nu_7$ associated hot bands are described in the companion paper [3]. As mentioned previously, several perturbations were observed during the investigation of the ν_2 band, that could not be accounted for. For this reason we used, whenever possible, the 2^1 (or the 2^16^1 or 2^19^1) experimental energy levels instead of the calculated ones, during the computation of line positions, and the same strategy was adopted for the $\nu_2+\nu_9-\nu_9$ and $\nu_2+\nu_6-\nu_6$ bands for the 2^16^1 or 2^19^1 energy levels. The ν_2 expansion of the transition moment operator (see Eq. 12 and Table 4] was used to compute the individual line intensities of the ν_2 band at 296K. These intensity parameters were used to deduced those associated to the three hot bands using Eq. 7 in Ref. [3?].

For both the ν_2 cold band and for $\nu_2+\nu_9-\nu_9$, $\nu_2+\nu_6-\nu_6$, and $\nu_2+\nu_7-\nu_7$ associated hot bands. the results of these computations at 5.8 µm, in term of number of lines, frequency range, lower and upper values of the individual line intensities, as well as total band intensities are given in Table 5. In order to enable comparisons, Table 5 also provides a short description of the HITRAN-GEISA list at 5.8 µm.

Uncertainties

The accuracy of the line positions is usually ~0.001 cm^{-1} and ~0.002 cm^{-1} for the ν_2 and $\nu_2+\nu_7-\nu_7$ bands, respectively. For the $\nu_2+\nu_9-\nu_9$, and $\nu_2+\nu_6-\nu_6$ hot bands, the accuracy is between

~0.003 to ~0.10 cm^{-1}, depending whether or not the considered line corresponds to an identified level in the 2^19^1 or 2^17^1 upper state.

For the intensities, since a detailed investigation of the high resolution spectra was performed, we are rather confident in the relative consistency of the intensities in the overall spectral region of the 5.8 µm region. Therefore, on a relative scale, the accuracy of the individual line intensities is between 5% and 15 % for the strongest and weakest lines, respectively.

Getting "absolute" intensities is always a difficult problem for HNO_3 which is known to be chemically unstable. The present experimental study was performed with a great care. Nevertheless, we estimate at 6% the relative uncertainty associated to the absolute intensities on average. This uncertainty number accounts for several sources of errors linked to:

- the knowledge of the HNO_3 partial pressure, accounting for the partial decomposition of the sample during the recording of the spectra (≈2%),
- the line intensity fitting and overall calculation processes (≈3%),
- the control of the temperature (0.4%),
- the path length uncertainty (0.4%).

Line shape parameters

The present work does not bring anything new in terms of line shape parameters. Therefore, for the preparation of our database at 5.8 µm, we implemented the line shape parameters which are presently quoted in the HITRAN database [1,10]. More explicitly the values γ_{Air}=0.098 cm^{-1}/atm, γ_{Self}=0.8070 cm^{-1}/atm, and n=0.75 were quoted for the air and self pressure broadening parameters, and for the temperature dependent parameters of the air pressure broadening parameters. Finally, the air pressure-induced line shifts are set everywhere at zero.

Computation of the band intensities:

By summing on these ν_2 individual intensities, we computed the ${}^{GEISA-21}S_{\nu 2}(296K)$ band intensity of the ν_2 band, which is:

$${}^{GEISA-21}S_{\nu 2}(296K) = 4.015 \times 10^{-17} (\pm 6\ \%)\ cm^{-1}/\ (molecule.cm^{-2}) \text{ at } 296\ K \quad \text{Eq.(12)}$$

According to Eq. (10), this corresponds to a "GEISA-21" computed integrated band intensity (IBI) at 5.8 µm of:

$$^{GEISA-21}S_{Tot}^{5.8\mu m}(296K) = 5.275\ ^{17}(\pm 6\ \%) \times 10^{-17}\ cm^{-1}/(molecule.cm^{-2}) \text{ at } 296\ K \qquad \text{Eq.(13)}$$

As discussed in Ref. [3], the GEISA-21 linelist includes contributions from the $\nu_2+\nu_9-\nu_9$, $\nu_2+\nu_7-\nu_7$, and $\nu_2+\nu_6-\nu_6$ hot bands in addition to those of the ν_2 band. Table 5 of the present paper summarizes shortly the results of these calculations. When summing on the individual line intensities present in GEISA-21 (cold and three hot bands for $H^{14}N^{16}O_3$), one gets the value:

$$^{GEISA-21}S_{\nu_2+3hots}(296K) = 4.83 \times 10^{-17}\ cm^{-1}/(molecule.cm^{-2}) \text{ at } 296K \qquad \text{Eq.(14)}$$

Of course, the contributions from the higher order hot bands for $H^{14}N^{16}O_3$ and from the other isotopic species are still missing in the GEISA-21 linelist.

VI Validations

Comparison with the existing band intensities measurements:

It is time to compare the value of the $^{GEISA-21}S_{Tot}^{5.8\mu m}(296K)$ Integrated Band Intensity (IBI) at 5.8 µm calculated during this work. This value is slightly weaker than the measured value achieved during the low resolution measurements of Chackerian et al. [8] (see Eq. (2)). More precisely, the ratio, $^{Low}_{GEISA-21}r_{5.8\mu m}(296K)$, between the low resolution measured [8] and the GEISA-21's integrated band intensities at 5.8 µm is:

$$^{Low}_{GEISA-21}r_{5.8\mu m}(296K) = {}^{Low}S_{Tot}^{5.8\mu m}(296K) / {}^{GEISA-21}S_{Tot}^{5.8\mu m}(296K) = 1.08\ (+/-\ 10\%) \qquad \text{Eq.(15)}$$

Thus, for the ν_2 band, the line intensities quoted in our new GEISA-21 linelist are, in general, about 8% weaker than those presented in the HITRAN-GEISA linelist. This is because this latter linelist was calibrated in intensity relative to the PNNL cross sections [8].

However, considering the uncertainties affecting the present measurements (about 6%) and those affecting Chackerian's band intensities at 5.8 µm [8] (about 3%, according to ref [8]) we consider that these experimental data are in reasonable agreement.

We expect that future atmospheric HNO_3 retrievals, using stratospheric spectra recorded simultaneously the 5.8 µm spectral region and the 11 µm and/or the 7.6 µm regions will bring a complementary information. One can mention, for example the ACE-FTS Fourier transform spectrometer on board the SCISAT satellite [5] or the balloon-borne JPL MkIV interferometer [14].

Comparison with the PNNL cross section data

The goal of this sub-section is to compare to the PNNL cross sections at 296K [8] to calculations using the HITRAN-GEISA and GEISA-21 linelists. This inter-comparison is shown in panel (a) of Fig. 4. However, each of these linelists accounts only for part of the infrared signature of HNO_3 at 5.8 µm, whereas the PNNL cross sections also include contributions from (all) hot bands and from minor isotopic species.

For the HITRAN-GEISA database, the global contribution of these "missing data" can be numerically computed by the factor ${}^{\text{HIT-GEIS}}\text{Factor}_{\text{Missing}}(296\text{K})$ defined here as the ratio (integrated band intensity / band intensity in HITRAN-GEISA) as (see Eq. (11):

$${}^{\text{HIT-GEIS}}\text{Factor}_{\text{Missing}}(296\text{K}) = \left({}^{\text{Low}}S_{\text{Tot}}^{5.8\mu\text{m}}(296K)\right) / \left({}^{HIT-GEIS}S_{\nu_2}(296K)\right) \approx 1.30 \qquad \text{Eq.(16)}$$

On the other hand, our GEISA-21 is more extended than HITRAN-GEISA, but still not complete. Using Eqs. (12) and (13) a similar "missing" factor can be defined as : :

$${}^{\text{GEISA-21}}\text{Factor}_{\text{Missing}}(296\text{K}) =$$

$$\left({}^{GEISA-21}S_{\text{Tot}}^{5.8\mu\text{m}}(296\text{K}) / {}^{GEISA-21}S_{\nu_2+3\text{hots}}^{5.8\mu\text{m}}(296\text{K})\right) \approx 1.09 \qquad \text{Eq.(17)}$$

In order to document the characteristics of the HITRAN-GEISA and GEISA-21 linelists, we multiplied the corresponding computed cross-sections by the correcting factors, ${}^{\text{HIT-GEIS}}\text{Factor}_{\text{Missing}}(296\text{K})$ and ${}^{\text{GEISA-21}}\text{Factor}_{\text{Missing}}(296\text{K})$, respectively. The (observed-calculated) results are presented in panels (b) of Fig. 4. The agreement between the observed and calculated signal is clearly better for GEISA-21 than for HITRAN-GEISA.

For example, in the 1709 cm^{-1} spectral region, the A- type Q structure of the ν_2 band leads to an error signature which is quite obvious for HITRAN-GEISA, but disappearing in GEISA-21.

We notice that the GEISA-21 computed cross sections are globally weaker by ~8% than those of PNNL. The only exception occurs in the far R- branch (1730-1740 cm^{-1}), where the GEISA-21-based cross-sections are slightly larger than those of the PNNL. We checked our line intensities measurements in that region of our high-resolution spectra, but could not detect a possible source of error.

Comparison with the existing line by line intensities measurements:

To our knowledge, only two line-by-line intensity measurements have been previously performed for the ν_2 band of HNO_3. Both papers [24; 25], which use tunable diode laser techniques, explore portions of the ν_2 R branch and give a list of experimental line positions and intensities. We restrict this inter-comparison to the experimental data corresponding to unblended lines for which HITRAN-GEISA or GEISA-21 proposes unambiguous ν_2 assignments. One notices that, in these microwindows, the intensity ratio between HITRAN-GEISA and GEISA-21 is almost constant (about 1.08).

The first paper [24] analyzes the 1718.97 cm^{-1} to 1729.57 cm^{-1} spectral region. Although the line position calibration is not perfect, it is clear that Bair and Brokman's measured intensities [24] are significantly stronger than those in HITRAN-GEISA, with a (non constant) intensity ratio ranging between 1.5 and 2.0.

The second paper [25] concerns the 1720.52 – 1724.79 cm^{-1} spectral region. We observed that these experimental intensities are systematically weaker than those of HITRAN-GEISA with an intensity ratio ranging between 0.55 to 0.67. This is surprising, considering that May et al. claimed that their measured line intensities are consistent with the band intensity measurements performed by Giver et al. [23][2].

We conclude that these diode laser measurements [24, 25] cannot be used faithfully to check the validity of this work.

[2] We mentioned previously that the band intensities of Giver et al. [22] and of Chackerian et al [8] are in excellent agreement.

VII Comparison between the observed and calculated spectra at high resolution

Laboratory spectra

Fig. 5 gives an overview of spectrum FTS2-3@223K, together with the differences (observed – calculated spectra) that one can obtain using the HITRAN-GEISA and GEISA-21 linelists. Also Figs. 2, 6, and 7 compare the observed and calculated spectra in several spectral regions of the 5.8 μm absorption bands. Other comparisons are given in Figs. 9 and 10 of the companion paper [3] describing first part of this work. In all cases, GEISA-21 proves to be more accurate and complete than HITRAN-GEISA.

Balloon-borne solar spectra recorded by the MkIV instrument [14] in the lower stratosphere

It is important to estimate the impact of this new linelist for the atmospheric retrievals. Fig. 8 compares the spectral fit to a MkIV balloon spectrum using the HITRAN 2016 HNO_3 linelist (left panel) and the present work (right panel). It is clear that the agreement between observed and calculated spectra is significantly better when using the new GEISA-21 linelist.

Conclusion

In this work, we perform an extended analysis of the ν_2 band of HNO_3 using a large set of Fourier transform spectra recorded at high resolution. As mentioned by previous authors, this band is weakly perturbed. A large set of individual line intensities were measured and, in this way, it was possible to prove for the first time that the (mainly) B–type ν_2 band also possesses a weak A–type component. However, the overall intensities achieved in this way are, on average, about 8% weaker than those quoted in HITRAN or in GEISA. This work complements a companion investigation [3] that deals with the first three hot bands. In this way, a comprehensive list of line positions and intensities was generated for the ν_2, $\nu_2+\nu_9-\nu_9$, $\nu_2+\nu_7-\nu_7$, and $\nu_2+\nu_6-\nu_6$ bands in the 5.8 μm region. This line list is of potential use for the temperature conditions encountered in the Earth atmosphere. For higher temperatures, ab initio calculations have been attempted to provide extended linelists [28, 29], but it should be kept in mind that nitric acid is unstable and decomposes well before reaching these temperatures [30].

Supplementary data:

- The list of assignments
- The results of the final energy level computation
- The final "GEISA-21" linelist for HNO_3 at 5.8 µm, which includes lines from the ν_2 band together with those of the $\nu_2+\nu_9-\nu_9$, $\nu_2+\nu_6-\nu_6$, and $\nu_2+\nu_7-\nu_7$ associated hot bands.

ACKNOWLEDGMENTS

The authors acknowledge support from ANR (project QUASARS-19-CE29-0013-01) and Synchrotron SOLEIL (projects 99180072 and 99200018). This work was also financially supported by the CNES through the project IASI-NG. Part of this work was performed at the Jet Propulsion Laboratory, California Institute of Technology, under contract with NASA.

REFERENCES

[1] I.E. Gordon, L.S. Rothman, C. Hill, R.V. Kochanov, Y. Tana, P.F. Bernath, M. Birk, V. Boudon, A. Campargue, K.V. Chance, B.J. Drouin, J.-M. Flaud, R.R. Gamache, J.T. Hodges, D. Jacquemart, V.I. Perevalov, A. Perrin, K.P. Shine, M.A. Smith, J. Tennyson, G.C. Toon, H. Tran, V.G. Tyuterev, A. Barbe, A.G. Csaszar, V.M. Devi, T. Furtenbacher, J.J.Harrison, J.M.Hartmann, A. Jolly, T.J. Johnson, T.Karman, I. Kleiner, A.A. Kyuberis, J. Loos, O.M. Lyulin, S.T. Massie, S.N. Mikhailenko, N. Moazzen-Ahmadi, H. Muller, O.V. Naumenko, A.V. Nikitin, O.L. Polyansky, M. Rey, M. Rotger, S.W. Sharpe, K. Sung, E. Starikova, S.A. Tashkun, J. Vander Auwera, G. Wagner, J. Wilzewski, P. Wcisło, S. Yuh and E.J. Zak, *The HITRAN2016 molecular spectroscopic database.* J. Quant. Spectrosc. Radiat. Transf. **203**, 3–69 (2017).

[2] N. Jacquinet-Husson, R. Armante, N.A. Scott, A. Chedin, L. Crepeau, C. Boutammine, A. Bouhdaoui, C. Crevoisier, V. Capelle, C. Boonne,N. Poulet-Crovisier, A. Barbe,D.C. Benner, V. Boudon, L.R. Brown, J. Buldyreva, A. Campargue, L.H. Coudert, V.M. Devi,M.J. Down, B.J. Drouin, A. Fayt, C. Fittschen, J.-M. Flaud, R.R. Gamache, J.J. Harrison, C. Hill, O. Hodnebrog, S.M. Hu, D. Jacquemart, A. Jolly, E. Jimenez, N. Lavrentieva, A.W. Liu, L. Lodi, O.M. Lyulin, S.T. Massie, S. Mikhailenko, H.S.P. Muller, O.V. Naumenko, A. Nikitin, C.J. Nielsen, J. Orphal, V. Perevalov, A. Perrin, E. Polovtseva, A. Predoi-Cross, M. Rotger, A.A. Ruth, Y. Shanshan, K. Sung, S. Tashkun, J. Tennyson, V.G. Tyuterev, J. Vander Auwera, B. Voronin and A. Maki, *The 2015 edition of the GEISA spectroscopic database*. J. Mol. Spectrosc. **327**, 31–72 (2016).

[3] A. Perrin, L. Manceron, R.Armante, F. Kwabia-Tchana, P.Roy, D. Doizi, and G.C.Toon. *First analysis of the $\nu_2+\nu_7$ and $\nu_2+\nu_9$ and $\nu_2+\nu_6$ combination bands of HNO_3: evidence of perturbations due to large amplitude OH torsion in the 2^19^1 excited state.* Molecular Physics, this issue.

[4] D.Y Wang, M. Höpfner, C.E. Blom, W.E. Ward, H. Fischer, T. Blumenstock, F. Hase, C. Keim, G.Y. Liu, S. Mikuteit, H. Oelhaf, G. Wetzel, U. Cortesi, F. Mencaraglia, G. Bianchini, G. Redaelli, M. Pirre, V. Catoire, N. Huret, C. Vigouroux, M. De Maziére, E. Mahieu, P.

Demoulin, S. Wood, D. Smale, N. Jones, H. Nakajima, T. Sugita, J. Urban, D. Murtagh, C.D. Boone, P.F. Bernath, K.A. Walker, J. Kuttippurath, A. Kleinböhl, G. Toon, C. Piccolo. *Validation of MIPAS HNO_3 operational data.* Atmos. Chem. Phys. **7**, 4905–4934 (2007).

[5] M.A. Wolff, T. Kerzenmacher, K. Strong, K.A. Walker, M. Toohey, E. Dupuy, P.F. Bernath, C.D. Boone, S. Brohede, V. Catoire, T. von Clarmann, M. Coffey, W.H. Daffer, M. De Mazière, P. Duchatelet, N. Glatthor, D.W.T. Griffith, J. Hannigan, F. Hase, M. Höpfner, N. Huret, N.Jones, K. Jucks, A. Kagawa, Y. Kasai, I. Kramer, H. Küllmann, J. Kuttippurath, E. Mahieu, E.; G. Manney, C.T. McElroy, C. McLinden, Y. Mébarki, S. Mikuteit, D. Murtagh, C. Piccolo, P. Raspollini, M. Ridolfi, R. Ruhnke, M. Santee, C. Senten, D. Smale, C. Tétard, J. Urban, S. Wood. *Validation of HNO_3, $ClONO_2$, and N_2O_5 from the Atmospheric Chemistry Experiment Fourier Transform Spectrometer (ACE-FTS).* Atmos. Chem. Phys. **8**, 3529–3562 (2008).

[6] C. Wespes, D. Hurtmans, C. Clerbaux, M.L. Santee, R.V. Martin, P.F. Coheur. *Global distributions of nitric acid from IASI/MetOP measurements.* Atmos. Chem. Phys., **9**, 7949–7962 (2009).

[7] https://iasi-ng.cnes.fr/en/IASI-NG/index.htm

[8] C. Chackerian, S.W. Sharpe, T.A. Blake, *Anhydrous nitric acid integrated absorption cross sections: 820–5300 cm^{-1}*. J. Quant. Spectrosc. Radiat. Transf. **81**, 429-441 (2003).

[9] A.Perrin, J. Orphal, J.-M. Flaud, S. Klee, G. Mellau, H. Mäder, D. Walbrodt, M. Winnewisser. *New analysis of the ν_5 and $2\nu_9$ bands of HNO_3 by infrared and millimeter wave techniques: line positions and intensities*. J. Mol. Spectrosc. **228**, 375-391 (2004).

[10] J.-M. Flaud, G. Brizzi, M. Carlotti, A. Perrin, M. Ridolfi, *MIPAS database: Validation of HNO_3 line parameters using MIPAS satellite measurements.* Atmospheric Chemistry and Physics **6**, 5037-5048 (2006).

[11] H. Tran, G. Brizzi, L. Gomez-Martin, A. Perrin, F. Hase, M. Ridolfi, J.-M. Hartmann **.** *Validation of HNO_3 spectroscopic parameters using atmospheric absorption and emission measurements*. J. Quant. Spectrosc. Radiat. Transf. **110**, 109-117 (2009).

[12] A. Perrin. *New analysis of the ν_3 and ν_4 bands of HNO_3 in the 7.6 µm region*. J. Phys. Chem. A, **117**, 13236–13248 (2013).

[13] A. Perrin, J.-M. Flaud, M. Ridolfi, J. Vander Auwera, and M. Carlotti, *MIPAS database: new HNO_3 line parameters at 7.6 µm validated with MIPAS satellite measurements*. Atmos. Meas. Tech., 9, 2067.2076, (2016). www.atmos-meas-tech.net/9/2067/2016/ doi:10.5194/amt-9-2067-2016

[14] G.C. Toon. *The JPL MkIV interferometer*. Opt Photon News **2**, 19–21 (1991).

[15] A. Goldman, F.J. Murcray, R.D. Blatherwick, J.J. Kosters, D.G. Murcray, C.P. Rinsland, J.-M. Flaud, C. Camy-Peyret, *Stratospheric HNO_3 Measurements from 0.002 cm^{-1} Resolution Solar Occultation Spectra and Improved Spectroscopic Line Parameters in the 5.8-µm Region*, Journal of Geophysical Research **97**, 2561-2567 (1992).

[16] G.Toon, private communication.

[17] S.W.Sharpe, T.J. Johnson, R.L. Sams, P.M. Chu, G.C. Rhoderick, and P.A. Johnson. *Gas-phase databases for quantitative infrared spectroscopy*, Appl. Spectrosc. **58**, 1452–1465 (2004).

[18] A.G. Maki, *High-resolution measurements of the ν_2 band of HNO_3 and the ν_3 band of trans-HONO*, J. Mol. Spectrosc. **127**, 104-111 (1988)

[19] T.L.Tan, E.C.Looi, K.T. Lua, *Improved Spectroscopic Constants for the n2 infrared Band of HNO_3*. J. Mol. Spectrosc. **155**, 420-423 (1992).

[20] Watson, J.K.G. *Aspects of quartic and sextic centrifugal effects on rotational energy levels, Chap 1 In: Vibrational spectra and structure*, Vol **6**, A series of advances, Edited by: Durig, J.R. 1-89 (1977).

[21] A. G. Maki and W.M. B. Olson, *Infrared spectrum of the* ν_6, ν_7, *and* ν_8 *bands of* NHO_3 J. Mol. Spectrosc. **133**, 171-181 (1989).

[22] A. Goldman, T.G. Kyle, and F.S. Bonomo. *Statistical band model parameters and integrated intensities for the 5.9-μ, 7.5-μ, and 11.3-μ bands of* HNO_3 *vapor*, Appl. Opt., **10**, 65–73, (1971).

[23] L.P. Giver, F.P.J. Valero, D. Goorvitch, and F.S. Bonomo. *Nitric-acid band intensities and band-model parameters from 610 to 1760* cm^{-1}, J. Opt. Soc. Am. B, **1**, 715–722, (1984).

[24] C. H. Bair and P. Brockman, *High-resolution spectral measurement of the* HNO_3 *5.9-μm band using a tunable diode laser*. Appl. Opt. **18**, 4152-4162 (1979).

[25] R.D. May, C.R. Webster, L.T. Molina. *Tunable diode laser measurements of absolute linestrengths in the* HNO_3 ν_2 *band near 5.8 μm*. *J. Quant. Spectrosc. Radiat. Transf.* **38**, 381-388 (1987).

[26]. D. T. Petkie, P. Helminger, R. A.H. Butler, S. Albert, and F. C. De Lucia. *The millimeter and submillimeter spectra of the ground state and excited* $\nu9$, $\nu8$, $\nu7$, *and* $\nu6$ *vibrational states of* HNO_3. J. Mol. Spectrosc. **218,** 127-130 (2003).

[27] M. Carleer. *WSpectra: A Windows program to accurately measure the line intensities of high-resolution Fourier transform spectra.* SPIE Remote Sensing, **4168,** 337-43 (2001).

[28] A.I. Pavlyuchko, S.N. Yurchenko, J. Tennyson. *A hybrid variational- perturbation calculation of the ro-vibrational spectrum of nitric acid.* J. Chem. Phys. **142**, 094309 (2015).

[29] A.I. Pavlyuchko, S.N. Yurchenko, J. Tennyson. *ExoMol molecular line lists: XI The spectrum of nitric acid.* Mon. Not. R. Astron. Soc. 000, 1–5 (2012).

[30] C. Kato, K. Kiuchi, K. Sugimoto. *Thermodynamic study on redox reactions of boiling nitric acid solutions*. Corrosion Engineering **52**, 69-85 (2003)

Table 1

Experimental details of the spectra used in this study. The estimated uncertainties are given in parenthesis in the units of the last significant digits.

Spectrum	Spectral range (cm^{-1})	Path length (m)	Press. (hPa)	Temp. (K)	Number of averaged interferograms
FTS2-1@223K	1650-1760	2.72(1)	0.0085(5)	223 (1)	456
FTS2-2@223K	1650-1760	2.72(1)	0.0113(5)	223 (1)	408
FTS2-3@223K	1650-1760	2.72(1)	0.0288(5)	223 (1)	456
FTS2	1650-1750	2.72(1)	0.0269(10)	296 (1)	368
FTS26-27-29	2010-2440	16.32 (5)	1.1 (1)	250 (1)	480

Table 2.Band centers, rotational and quartic centrifugal constants (in cm^{-1}) for the ν_2 band.

			This work:	Tan et al. [19]
		Ground state [26]	2^1	2^1
$\mathbf{E_V}$			1709.56693(8)	1709.567256
A		0.43399982330	0.431725287(570)	0.431722 993(106)
B		0.40360999242	0.402831525(410)	0.402828787(71)
C		0.20883238263	0.208135989(320)	0.208134195(57)
Δ_K	$\times 10^6$	0.2464975	0.265161(680)	0.268361(104)
Δ_{JK}	$\times 10^6$	-0.15168080	-0.168872(530)	-0.172021(167)
Δ_J	$\times 10^6$	0.29708186	0.3037138(960)	0.301076(36)
δ_K	$\times 10^6$	0.2494516	0.2483774(340)	0.246281(74
δ_J	$\times 10^6$	0.12627092	0.1277192(900)	0.127785(15)
H_K	$\times 10^{11}$	0.411518	0.6615(480)	#
H_{KJ}	$\times 10^{11}$	-0.368588	-0.8175(650)	#
H_{JK}	$\times 10^{12}$	0.909863	3.318(260)	1.567(29)
H_J	$\times 10^{13}$	-0.1935	13.072(320)	-1.75l(60)
h_K	$\times 10^{12}$	1.7362	2.204(240)	#
l_K	$\times 10^{12}$	1.7362	(a)	1.664(55)
l_{JK}	$\times 10^{17}$	-1.9117	(a)	-1.049(24)
h_J	$\times 10^{15}$	1.151	(a)	
h_{JK}	$\times 10^{14}$	6.8647	(a)	
L_K	$\times 10^{16}$	-1.476	(a)	
L_{KKJ}	$\times 10^{16}$	1.1861	(a)	
l_{KJ}	$\times 10^{17}$	2.118	(a)	
l_{JK}	$\times 10^{17}$	-1.9117	(a)	

Part (2): Results of the energy levels calculation:

Total number of infrared levels	1697 [(b)]
$0. \times 10^{-3} \leq \delta < 1\times 10^{-3}$	90.63%
$1 \times 10^{-3} \leq \delta < 2\times 10^{-3}$	3.30%
$2 \times 10^{-3} \leq \delta < 3\times 10^{-3}$	1.71%
$3\times 10^{-3} < \delta < 70\times 10^{-3}$ [(b)]	4 .36%

Caption :

In Ref. [19] fixed to the ground state values [21]

[(a)]Values from ground state constants.

$\delta=|E_{Obs}-E_{Calc}|$: absolute value of the (observed – calculated) energy value, in cm^{-1}.

[(b)] The levels for which $\delta > 3\times 10^{-3}$ were not considered in the energy levels computation.

Table 3:

List of measured line intensities at 223K for the ν_2 band of $H^{14}N^{16}O_3$. J', Ka',K'c and J'', Ka'',K''c represent upper and lower state rotational quantum numbers. The "d" flag indicates the degenerate K_a or K_c values. Sigma: calculated line position (cm^{-1}). Int(Obs), Int(Calc): Observed and calculated line intensity in $cm^{-1}.atm^{-1}$ at 223K, O-C(%) difference in percentage, ΔInt/Int : estimated relative uncertainty in percentage (see text).

J'	Ka'	Kc'	J''	Ka''	Kc''	Sigma	Int(Obs)	ΔInt/Int(%)	Int(Calc)	O-C (%)
23	23	d	23	23	d	1708.3635	6.740E-02	11.1	7.350E-02	-9.0
24	23	d	24	23	d	1708.3690	6.710E-02	13.6	5.950E-02	11.3
25	23	d	25	23	d	1708.3762	4.670E-02	7.7	4.740E-02	-1.4
22	22	d	22	22	d	1708.4661	7.530E-02	8.1	7.970E-02	-5.9
23	22	d	23	22	d	1708.4714	5.590E-02	9.0	6.450E-02	-15.5
21	21	d	21	21	d	1708.5642	8.120E-02	8.3	8.580E-02	-5.7
22	21	d	22	21	d	1708.5691	8.490E-02	6.8	6.940E-02	18.3
19	19	d	19	19	d	1708.7466	9.570E-02	8.1	9.700E-02	-1.3
10	10	0	10	10	1	1709.3459	5.790E-02	6.9	5.090E-02	12.0
9	9	0	9	9	1	1709.3925	4.870E-02	12.8	4.770E-02	2.1
8	8	0	8	8	1	1709.4377	4.600E-02	15.3	4.360E-02	5.2
39	39	d	40	40	d	1671.5608	7.890E-02	10.6	6.880E-02	12.8
39	37	d	40	38	d	1672.2633	6.640E-02	12.0	6.400E-02	3.6
35	32	d	36	33	d	1676.6754	1.120E-01	12.3	1.200E-01	-6.8
34	33	d	35	34	d	1677.0308	1.580E-01	11.2	1.600E-01	-1.2
34	30	d	35	31	d	1678.0071	1.300E-01	5.3	1.260E-01	2.9
31	31	d	32	32	d	1679.7364	2.670E-01	9.3	2.660E-01	0.3
42	d	25	43	d	26	1682.1773	7.430E-02	14.7	7.590E-02	-2.2
43	d	28	44	d	29	1682.5826	8.880E-02	14.1	8.370E-02	5.7
41	d	24	42	d	25	1682.6780	8.980E-02	7.8	8.530E-02	5.0
48	d	39	49	d	40	1682.8818	7.890E-02	9.6	9.400E-02	-19.1
46	d	35	47	d	36	1682.9354	1.120E-01	10.5	9.310E-02	16.9
40	d	23	41	d	24	1683.1780	1.210E-01	6.9	9.550E-02	21.1
39	d	21	40	d	22	1683.2301	1.060E-01	7.4	9.610E-02	9.3
45	d	34	46	d	35	1683.4332	1.070E-01	10.8	1.050E-01	1.8
41	d	26	42	d	27	1683.5813	1.000E-01	10.7	1.060E-01	-5.6
46	d	37	47	d	38	1683.8755	1.120E-01	7.9	1.200E-01	-7.1
41	d	27	42	d	28	1684.0363	1.060E-01	11.0	1.180E-01	-11.0
40	d	25	41	d	26	1684.0784	1.130E-01	11.6	1.180E-01	-4.3
37	d	19	38	d	20	1684.2251	1.090E-01	9.2	1.180E-01	-8.2
42	d	30	43	d	31	1684.4563	1.240E-01	11.4	1.320E-01	-6.4
41	d	28	42	d	29	1684.4913	1.290E-01	10.6	1.320E-01	-1.9
39	d	24	40	d	25	1684.5740	1.400E-01	7.4	1.310E-01	6.4
39	d	25	40	d	26	1685.0254	1.850E-01	8.2	1.460E-01	21.3
37	d	21	38	d	22	1685.1139	1.530E-01	5.7	1.440E-01	5.6
36	d	19	37	d	20	1685.1627	1.420E-01	12.9	1.430E-01	-1.0
35	d	17	36	d	18	1685.2148	1.360E-01	10.7	1.420E-01	-4.3

36	d	20	37	d	21	1685.6087	1.440E-01	8.3	1.590E-01	-10.2
41	d	31	42	d	32	1685.8728	1.710E-01	13.1	1.850E-01	-8.3
40	d	29	41	d	30	1685.9026	2.270E-01	8.5	1.830E-01	19.4
36	d	21	37	d	22	1686.0524	1.890E-01	4.5	1.760E-01	7.1
41	d	32	42	d	33	1686.3367	1.920E-01	12.3	2.080E-01	-8.6
40	d	30	41	d	31	1686.3625	2.110E-01	9.3	2.050E-01	2.8
39	d	28	40	d	29	1686.3900	2.220E-01	12 .1	2.020E-01	8.9
32	d	14	33	d	15	1686.6862	1.980E-01	9.1	1.790E-01	9.5
40	d	31	41	d	32	1686.8248	2.380E-01	10.0	2.310E-01	3.2
39	d	29	40	d	30	1686.8514	2.080E-01	12.2	2.260E-01	-8.8
34	d	19	35	d	20	1687.0315	1.860E-01	9.4	2.090E-01	-12.2
33	d	17	34	d	18	1687.0768	2.050E-01	7.1	2.040E-01	0.3
32	d	15	33	d	16	1687.1248	2.110E-01	8.9	1.990E-01	5.8
31	d	13	32	d	14	1687.1732	1.760E-01	13.0	1.910E-01	-8.5
37	d	26	38	d	27	1687.3669	2.790E-01	7.3	2.440E-01	12.5
36	d	24	37	d	25	1687.3998	2.570E-01	10.8	2.400E-01	6.7
35	d	22	36	d	23	1687.4361	2.510E-01	12.6	2.350E-01	6.2
30	d	12	31	d	13	1687.6571	1.900E-01	10.2	2.020E-01	-6.2
38	d	29	39	d	30	1687.7974	2.980E-01	9.9	2.790E-01	6.5
37	d	27	38	d	28	1687.8228	2.590E-01	9.6	2.730E-01	-5.2
36	d	25	37	d	26	1687.8526	2.710E-01	9.8	2.670E-01	1.6
35	d	23	36	d	24	1687.8856	2.580E-01	11.2	2.610E-01	-1.3
32	d	17	33	d	18	1688.0043	2.410E-01	10.8	2.430E-01	-0.9
31	d	15	32	d	16	1688.0493	2.300E-01	10.0	2.350E-01	-2.3
30	d	13	31	d	14	1688.0953	2.210E-01	6.9	2.250E-01	-1.9
36	d	26	37	d	27	1688.3073	3.100E-01	9.3	2.970E-01	4.1
33	d	20	34	d	21	1688.4065	2.850E-01	11.1	2.770E-01	3.0
35	d	25	36	d	26	1688.7902	2.990E-01	7.9	3.230E-01	-8.1
34	d	23	35	d	24	1688.8199	3.000E-01	8.6	3.150E-01	-4.9
33	d	21	34	d	22	1688.8533	2.990E-01	10.4	3.060E-01	-2.4
29	d	13	30	d	14	1689.0152	2.610E-01	10.7	2.640E-01	-1.1
28	d	11	29	d	12	1689.0571	2.290E-01	10.5	2.470E-01	-7.8
33	d	22	34	d	23	1689.3018	3.650E-01	10.2	3.400E-01	7.0
32	d	20	33	d	21	1689.3349	3.190E-01	10.9	3.290E-01	-3.2
31	d	18	32	d	19	1689.3716	3.140E-01	11.7	3.190E-01	-1.4
30	d	16	31	d	17	1689.4110	2.930E-01	10.2	3.070E-01	-4.7
21	21	d	22	22	d	1689.5682	8.090E-01	6.4	7.970E-01	1.5
34	d	25	35	d	26	1689.7252	3.680E-01	8.7	3.890E-01	-5.8
33	d	23	34	d	24	1689.7520	4.010E-01	9.7	3.770E-01	6.0
31	d	20	32	d	21	1690.2609	3.850E-01	9.6	3.900E-01	-1.4
30	d	18	31	d	19	1690.2943	3.720E-01	6.6	3.750E-01	-0.9
29	d	16	30	d	17	1690.3307	3.590E-01	8.8	3.590E-01	-0.1
28	d	14	29	d	15	1690.3698	3.450E-01	8.5	3.420E-01	1.0
20	20	d	21	21	d	1690.5275	9.080E-01	7.4	8.540E-01	6.0
33	d	25	34	d	26	1690.6580	4.050E-01	7.6	4.670E-01	-15.3
32	d	23	33	d	24	1690.6813	4.280E-01	8.8	4.500E-01	-5.0

31	d	21	32	d	22	1690.7083	4.410E-01	7.1	4.320E-01	1.9
25	16	9	26	17	10	1690.9145	1.370E-01	8.4	1.320E-01	4.0
21	17	4	22	18	5	1691.0337	1.530E-01	7.0	1.610E-01	-5.5
32	d	24	33	d	25	1691.1339	4.510E-01	7.5	5.000E-01	-10.8
20	17	3	21	18	4	1691.4076	2.270E-01	14.0	2.390E-01	-5.2
29	d	19	30	d	20	1691.6590	5.720E-01	8.0	4.870E-01	14.9
28	d	17	29	d	18	1691.6895	4.510E-01	9.3	4.640E-01	-2.8
24	d	9	25	d	10	1691.8260	3.620E-01	10.4	3.410E-01	5.9
26	d	14	27	d	15	1692.1962	4.570E-01	8.3	4.560E-01	0.1
18	18	d	19	19	d	1692.4326	9.670E-01	6.0	9.580E-01	1.0
29	d	21	30	d	22	1692.5535	5.390E-01	9.2	5.980E-01	-11.0
26	d	15	27	d	16	1692.6348	4.900E-01	7.2	5.060E-01	-3.2
17	17	d	18	18	d	1693.3788	9.900E-01	5.9	1.000E+00	-1.1
27	d	19	28	d	20	1693.4931	6.120E-01	8.3	6.590E-01	-7.8
26	d	17	27	d	18	1693.5173	5.920E-01	7.8	6.200E-01	-4.8
18	14	4	19	15	5	1694.2416	1.790E-01	12.8	1.580E-01	11.6
24	d	16	25	d	17	1694.8923	6.550E-01	7.8	7.340E-01	-12.1
15	15	d	16	16	d	1695.2578	9.640E-01	7.0	1.060E+00	-10.4
22	d	13	23	d	14	1695.3801	6.610E-01	6.5	6.890E-01	-4.2
38	d	29	38	d	28	1696.1567	8.950E-02	11.0	8.820E-02	1.5
28	d	25	28	d	24	1698.6104	1.810E-01	10.4	1.650E-01	8.8
34	d	21	34	d	20	1699.6503	1.530E-01	8.5	1.450E-01	4.9
35	d	20	35	d	19	1699.9570	1.060E-01	15.5	1.280E-01	-20.7
22	d	20	22	d	19	1700.9739	2.130E-01	9.4	2.070E-01	2.6
36	d	18	36	d	17	1700.6815	1.060E-01	7.4	1.100E-01	-3.5
23	d	19	23	d	18	1701.3014	3.130E-01	9.8	2.790E-01	10.8
32	d	16	32	d	15	1701.8488	2.040E-01	10.6	1.860E-01	8.9
28	21	7	28	22	6	1706.8707	1.860E-01	10.4	1.920E-01	-3.1
16	d	8	16	d	9	1712.7486	5.760E-01	8.2	6.070E-01	-5.3
17	d	10	17	d	11	1713.5726	5.850E-01	9.1	5.310E-01	9.2
29	d	17	29	d	18	1715.7987	2.970E-01	9.7	2.770E-01	6.8
23	d	20	23	d	21	1717.6402	1.800E-01	11.2	2.090E-01	-16.4
30	d	22	30	d	23	1717.9663	2.550E-01	12.5	2.210E-01	13.3
23	d	21	23	d	22	1718.0930	1.650E-01	9.6	1.510E-01	8.6
30	d	24	30	d	25	1718.8807	2.130E-01	12.1	1.940E-01	8.8
30	d	25	30	d	26	1719.3401	1.850E-01	10.4	1.760E-01	4.8
16	d	8	15	d	7	1719.4731	6.710E-01	5.8	7.060E-01	-5.2
19	d	9	18	d	8	1721.4252	6.480E-01	8.1	6.280E-01	3.0
21	d	11	20	d	10	1722.1605	6.910E-01	8.9	6.560E-01	5.0
24	d	14	23	d	13	1723.2594	6.480E-01	8.1	6.460E-01	0.2
24	d	12	23	d	11	1724.0704	5.390E-01	9.0	5.260E-01	2.4
24	d	11	23	d	10	1724.4847	4.840E-01	9.2	4.720E-01	2.6
28	d	18	27	d	17	1724.7092	5.760E-01	9.4	5.710E-01	0.9
27	d	16	26	d	15	1724.7447	5.620E-01	9.1	5.390E-01	4.0
26	d	14	25	d	13	1724.7870	5.360E-01	8.4	5.050E-01	5.8
24	d	10	23	d	9	1724.9086	4.540E-01	10.2	4.190E-01	7.7

28	d	17	27	d	16	1725.1031	5.260E-01	7.4	5.180E-01	1.5
31	d	22	30	d	21	1725.3963	5.530E-01	8.6	5.410E-01	2.1
29	d	18	28	d	17	1725.4604	4.600E-01	8.3	4.950E-01	-7.6
28	d	16	27	d	15	1725.5002	4.840E-01	9.7	4.700E-01	2.9
27	d	14	26	d	13	1725.5473	5.030E-01	9.0	4.430E-01	12.0
34	d	26	33	d	25	1726.0838	4.540E-01	10.0	4.950E-01	-9.1
28	d	14	27	d	13	1726.3056	4.180E-01	7.4	3.860E-01	7.6
33	d	23	32	d	22	1726.4912	4.240E-01	9.8	4.320E-01	-1.9
21	21	d	20	20	d	1726.6945	9.210E-01	5.8	9.800E-01	-6.4
30	d	16	29	d	15	1727.0038	3.650E-01	8.4	3.520E-01	3.6
37	d	26	36	d	25	1728.2691	2.890E-01	9.7	2.870E-01	0.6
39	d	28	38	d	27	1728.9558	2.440E-01	9.6	2.400E-01	1.5
36	d	22	35	d	21	1729.0735	2.330E-01	12.9	2.320E-01	0.6
41	d	31	40	d	30	1729.2694	2.100E-01	10.0	2.210E-01	-5.4
39	d	26	38	d	25	1729.7109	2.000E-01	8.7	1.950E-01	2.5
43	d	33	42	d	32	1729.9496	1.740E-01	8.6	1.800E-01	-3.7
41	d	29	40	d	28	1730.0139	1.730E-01	7.0	1.780E-01	-2.7
41	d	27	40	d	26	1730.7631	1.360E-01	11.7	1.440E-01	-5.8
44	d	32	43	d	31	1731.0201	1.320E-01	13.7	1.290E-01	2.5
45	d	33	44	d	32	1731.3530	1.090E-01	11.4	1.150E-01	-5.3
51	d	42	50	d	41	1732.2601	9.140E-02	13.7	7.950E-02	13.0
47	d	34	46	d	33	1732.3784	7.300E-02	13.2	8.030E-02	-10.1
51	d	40	50	d	39	1732.9657	5.920E-02	4.8	6.120E-02	-3.3
49	d	34	48	d	33	1733.7576	4.440E-02	13.5	4.910E-02	-10.5
41	41	d	40	40	d	1741.1269	7.100E-02	11.4	7.400E-02	-4.2
41	40	d	40	39	d	1741.1514	7.100E-02	10.0	7.180E-02	-1.1
42	42	d	41	41	d	1741.7967	6.050E-02	9.5	6.080E-02	-0.5
42	41	d	41	40	d	1741.8257	7.470E-02	11.0	5.920E-02	20.8
42	40	d	41	39	d	1741.8516	5.560E-02	6.4	5.700E-02	-2.6

Table 4:

Expansion of the transition moment operator of the ν_2 band (see Eq. 11).

	Operator	Values[(a)]
${}^{2,0}\mu_1^B$	$\varphi_{x=B}$	0.2548(11) D
${}^{2,0}\mu_2^B$	$\varphi_x \mathbf{J}^2$	$0.552(45)\times10^{-5}$ D
${}^{2,0}\mu_1^A$	$\varphi_{z=A}$	0.05739(66) D
${}^{2,0}\mu_4^A$	$1/2\left(\{\varphi_x, iJ_y\} + \{i\varphi_y, J_x\}\right)$	$-0.740(64)\times10^{-3}$ D

(a) Values (in Debye, 1 D = 3.33564×10^{-30} C m) resulting from the least squares fit calculation performed on the experimental intensities. The quoted errors (in parentheses) are one standard deviation.

Table 5

The GEISA-21 database in the 5.8 μm region. Vib' and Vib'' are the upper and lower state vibrational state. Nb is the number of lines. Sigma min and max are the lower and upper wavenumber range (in cm^{-1}). Band int, Int_{Min}, Int_{Max} are the band intensity, the minimum and maximum value of the line strength (in $cm^{-1}/(molecule.cm^{-2})$ at 296 K.

Vib'	Vib''	Nb	Band intensity	Sigma min	Sigma Max	Int min	Int Max
GEISA-21	(This work)						
2^1	Ground	33726	0.402E-16	1619.86	1790.14	0.1E-23	0.36E-19
2^19^1	9^1	28678	0.413E-17	1635.92	1771.52	0.1E-23	0.25E-20
2^16^1	6^1	17173	0.170E-17	1630.38	1766.97	0.1E-23	0.16E-20
2^17^1	7^1	18705	0.237E-17	1638.17	1766.27	0.1E-23	0.22E-20
Total		98282	0.483E-16				
HITRAN Or GEISA							
2^1	Ground	32336	0.438E-16	1650.01	1769.98	0.2E-23	0.42E-19

List of Figures

Fig 1: Overview of the four spectra recorded during this work in the 5.8 µm region. The experimental details are given in Table 1.

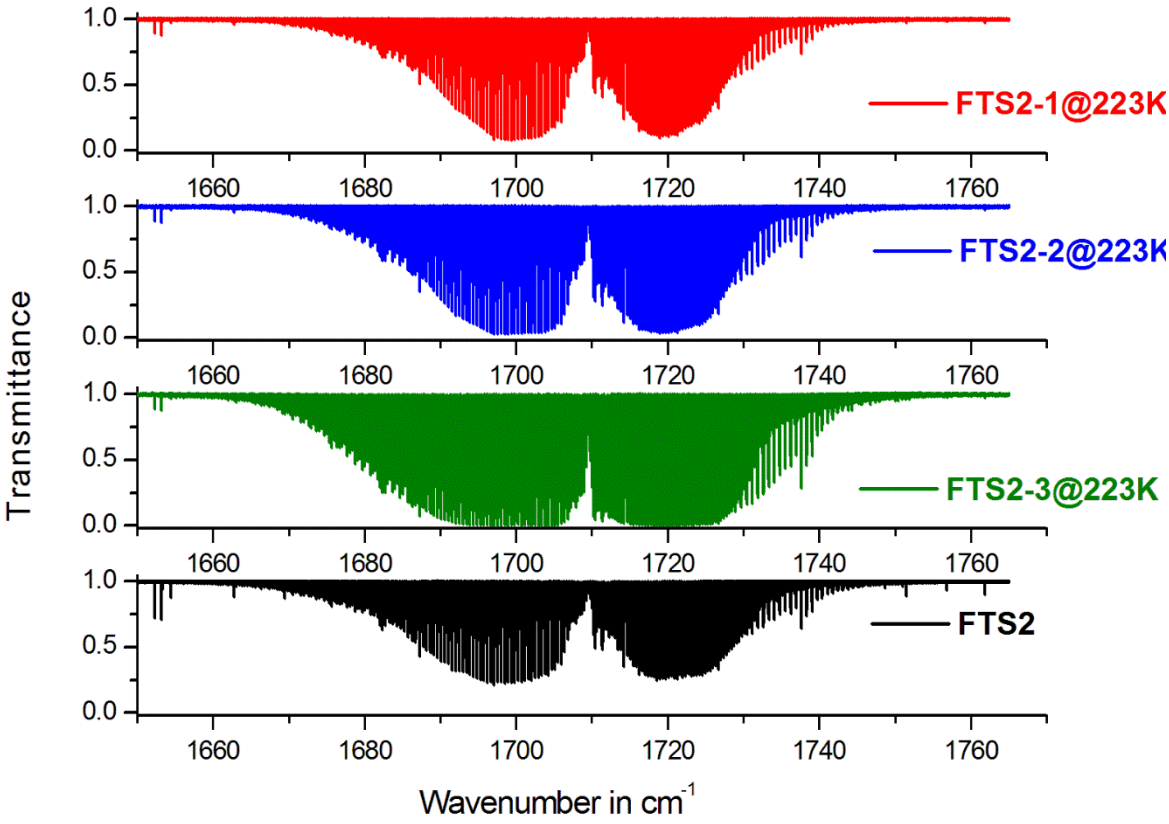

Fig 2: Central part of the A-type Q branch of the (mainly B-type) ν_2 band of HNO_3, and comparison of the present linelist with our spectrum "FTS2-3@223K". The assignments for the $^{Q}Q(K_a=J)$ transitions are also shown (triangles). A comparison with the model provided by the HITRAN-GEISA linelist is also given.

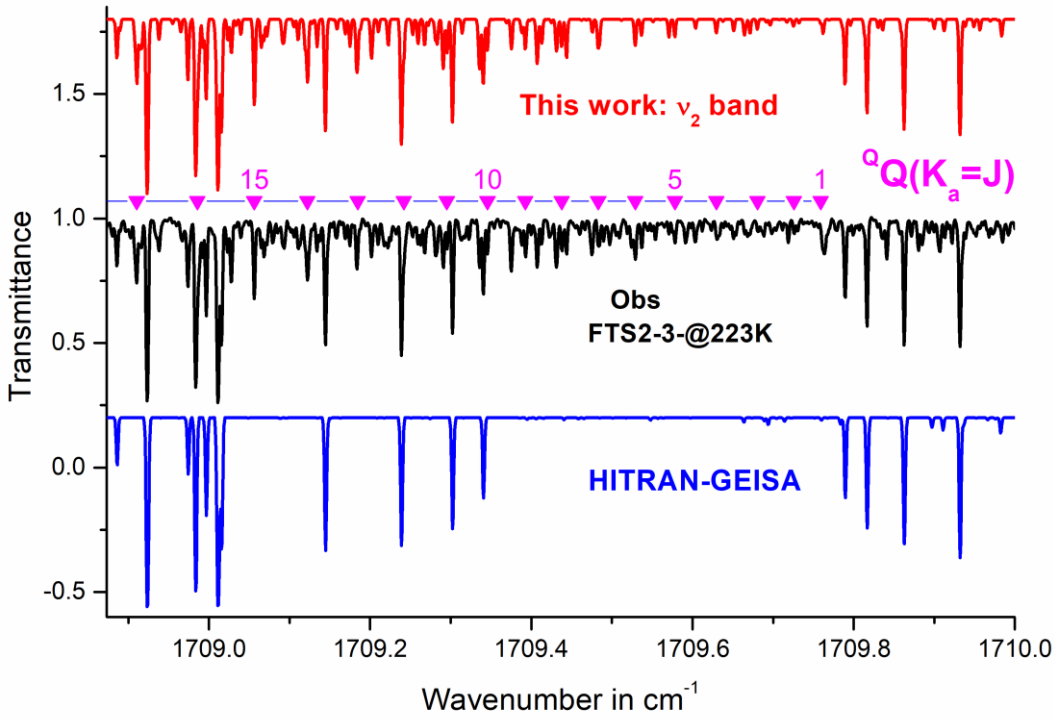

Figure 3 : Examples of spectral absorbance fits in the P-branch (left), the Q-branch (middle), and in the R-branch (right) of the ν_2 band. Black lines are the measured spectra (FTS2-2 and FTS2-3), red squares correspond to the fits and red lines show the residuals (calculated-measured), as obtained with the OPUS and WSpectra softwares. The retrieved integrated naperian absorbances are 7.1 and 2.8× 10^{-3} cm^{-1} for the 1690.5272 cm^{-1} line (left panel), 4.8 and 1.7× 10^{-3} cm^{-1} for the 1713.5726 cm^{-1} line (middle panel) and 4.2 and 1.6 × 10^{-3} cm^{-1} for the 1725.1031 cm^{-1} line (right panel).

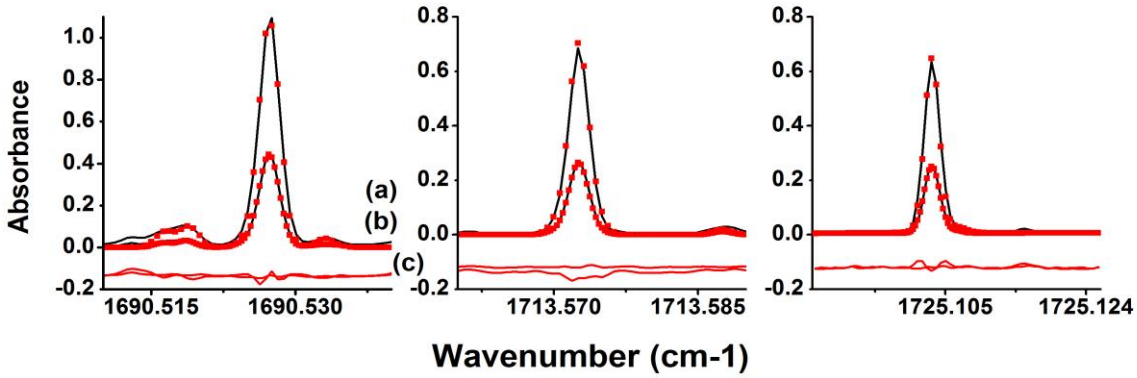

Fig. 4: (a) Comparison of the PNNL cross sections (in cm^2/molecule at 296K) [8] with their corresponding values using the HITRAN-GEISA linelist and the GEISA-21 linelist.

(b) (Observed – (corrected) calculated values) using HITRAN-GEISA and GEISA-21, when accounting for the missing hot bands: the HITRAN-GEISA and GEISA-21 computed cross sections are multiplied by $^{HIT\text{-}GEIS}Factor_{Missing}$ =1.30 and $^{GEISA\text{-}21}Factor_{Missing}$ =1.09 correcting factors, respectively.

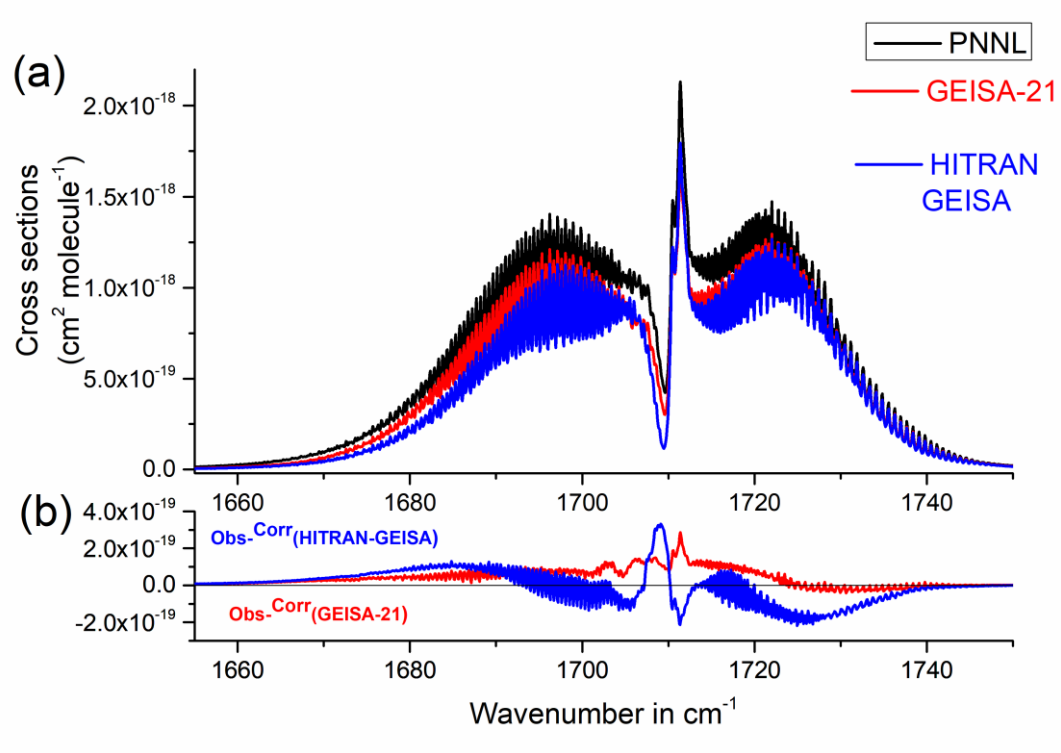

Fig. 5: Overview of the HNO_3 spectrum recorded at 223K in the 5.8 µm region (FTS2-3@223K). The (Observed – Calculated) signals are compared for the old (HITRAN-GEISA) and new (GEISA-21) line lists. Lines belonging to water vapor are shown in the lower trace (offset for clarity). Both computations account for the presence of water vapour in the absorption cell.

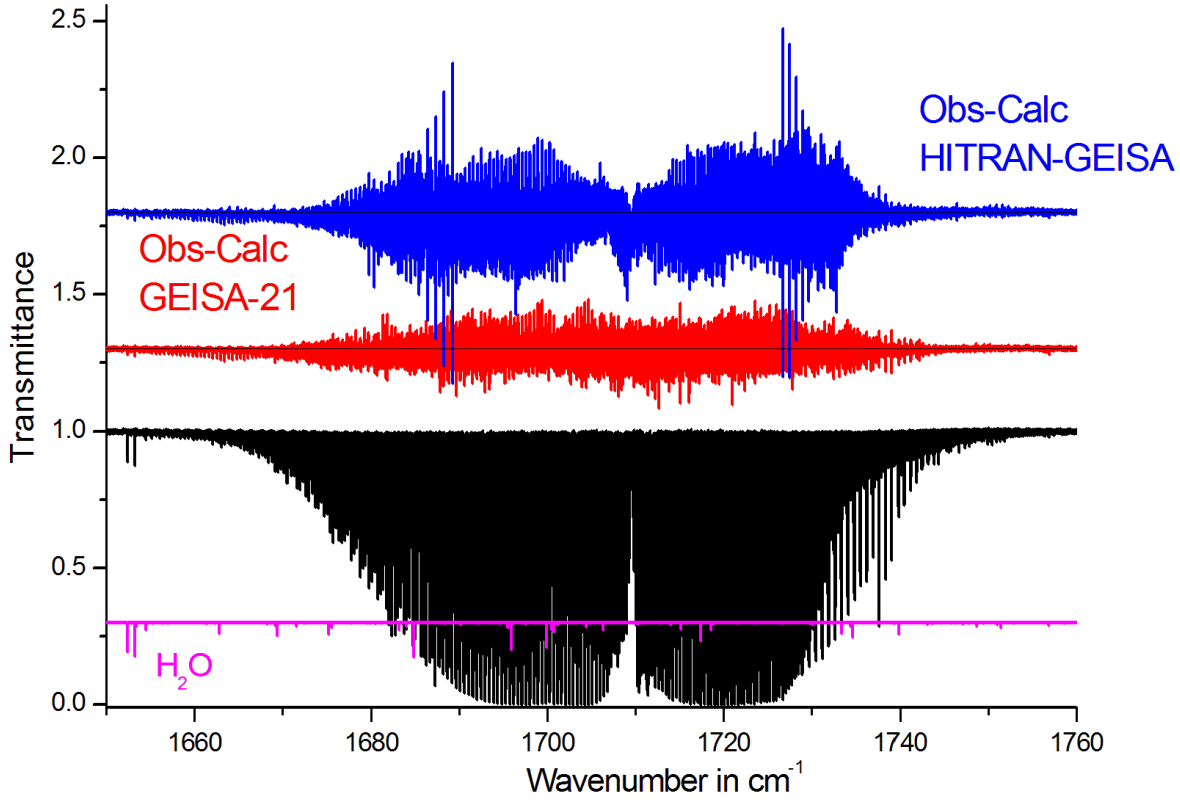

Fig 6: Portion of the R-branch of the ν_2 band of HNO_3 near 1726.7 to 1727.52 cm^{-1} (FTS2-3@223K). The (Observed-Calculated) predictions provided by HITRAN-GEISA and the present work for the ν_2 band are compared. In the new list, the line positions were calculated using the observed 2^1 energy levels instead of the computed ones, for perturbed lines. The (Obs-Calc) traces are offset for clarity.

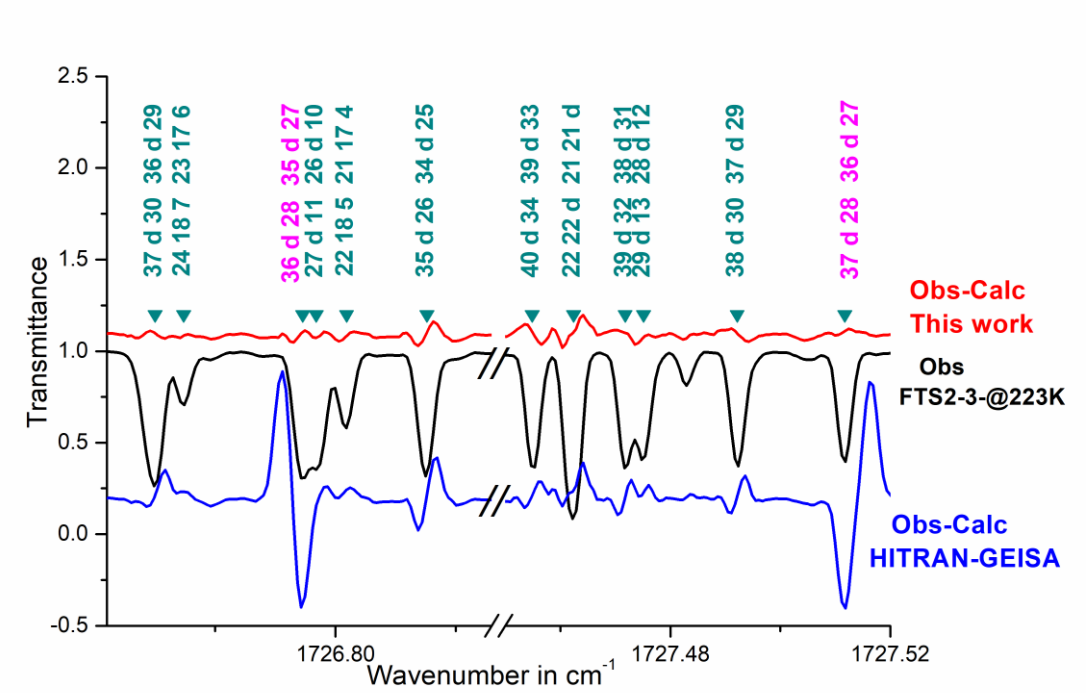

Fig 7. Portion of the R- branch of the ν_2 band of HNO_3 near 1732.1 cm^{-1} (FTS2-3@223K). The (Observed-Calculated) predictions provided by the HITRAN-GEISA and the present work for the ν_2 band are compared. In the new list, the line positions were calculated using the observed 2^1 energy levels instead of the computed ones, for pertubed lines. The (Obs-Calc) traces are offset for clarity.

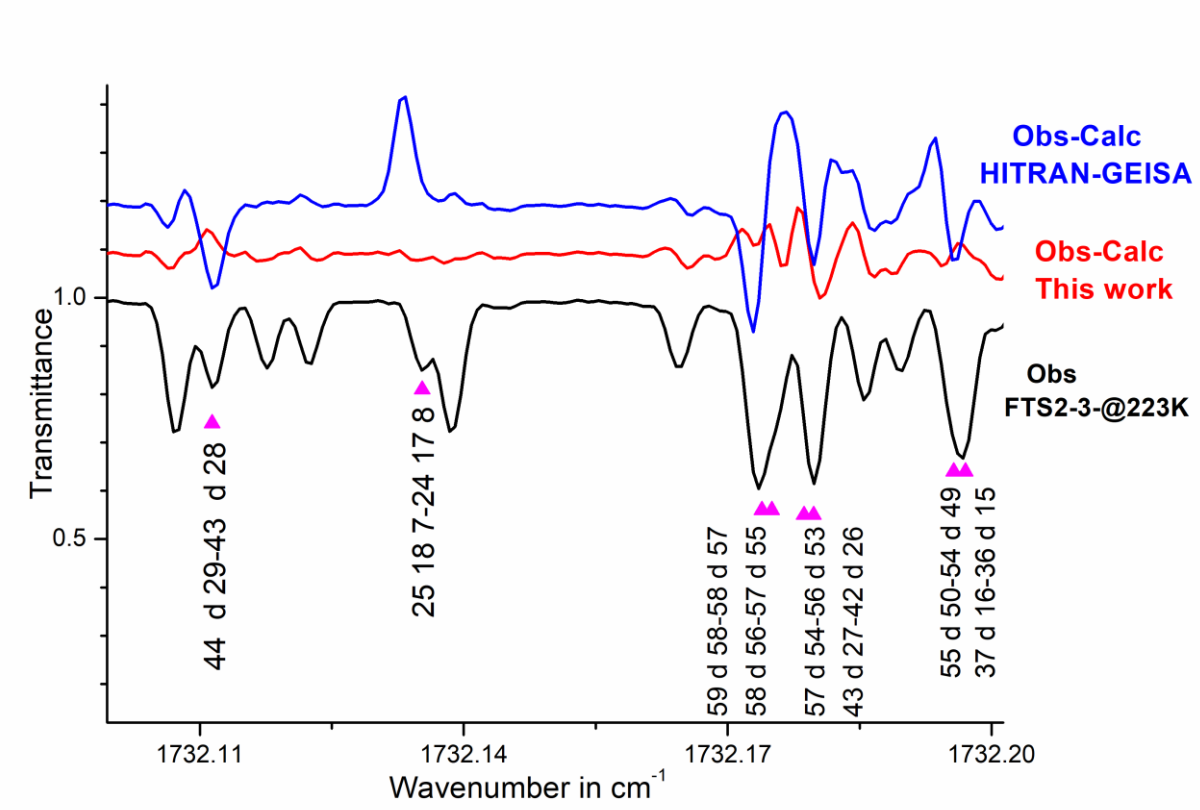

Figure 8. Example of a spectral fit to a MkIV balloon spectrum using the HITRAN 2016 HNO_3 linelist (left panel) and the present work (right panel). Black diamonds represent the measured spectrum, the black line the fitted calculation, and the red lines the contribution of HNO_3. This particular spectrum was measured at 20.3 km tangent altitude above Alaska in 1997, where the tangent temperature and pressure were 230K and 50 mbar. The upper panels display the residuals (Obs-Calc.); note the scale change between left and right residuals. The main absorbers in this region are HNO_3, H_2O, and O_3, but the spectroscopy of these other gases was unchanged, so the differences between the left- and right-hand panels are entirely attributable to HNO_3 spectroscopy changes.